Petroleum Science 20 (2023) 447–459

Contents lists available at ScienceDirect

Petroleum Science

journal homepage: www.keaipublishing.com/en/journals/petroleum-science

Original Paper

THM coupled analysis of cement sheath integrity considering well loading history

Xiao-Rong Li [a, *], Chen-Wang Gu [b], Ze-Chen Ding [a], Yong-Cun Feng [b]

[a] College of Safety and Ocean Engineering, China University of Petroleum (Beijing), Beijing, 102249, China
[b] College of Petroleum Engineering, China University of Petroleum (Beijing), Beijing, 102249, China

ARTICLE INFO

Article history:
Received 31 March 2022
Received in revised form
2 September 2022
Accepted 4 September 2022
Available online 9 September 2022

Edited by Yan-Hua Sun

Keywords:
Cement sheath integrity
Thermal–hydrological–mechanical
Whole life cycle
Cement sheath shrinkage
Initial stresses

ABSTRACT

The cement sheath is the heart of any oil or gas well for providing zonal isolation and well integrity during the life of a well. Loads induced by well construction operations and borehole pressure and temperature changes may lead to the ultimate failure of cement sheath. This paper quantifies the potential of cement failure under mechanically and thermally induced stress during the life-of-well using a coupled thermal–hydrological–mechanical (THM) modeling approach. A staged finite-element procedure is presented considering sequential stress and displacement development during each stage of the well life, including drilling, casing, cementing, completion, production, and injection. The staged model quantifies the stress states and state variables, e.g., plastic strain, damage, and debonding at cement/rock or cement/casing interface, in each well stage from simultaneous action of *in-situ* stress, pore pressure, temperature, casing pressure, and cement hardening/shrinkage. Thus, it eliminates the need to guess the initial stress and strain state before modeling a specific stage. Moreover, coupled THM capabilities of the model ensure the full consideration of the interaction between these influential factors.

1. Introduction

The integrity of the cement sheath is critical for protecting the casing and ensuring zonal isolation during the life of a well. Cement sheath may lose integrity due to the development of shear and tensile cracks within the cement sheath, or debonding at cement–casing or cement–formation interfaces, as shown in Fig. 1. The main reasons causing these failure modes include the initial stress concentration induced by *in-situ* stresses and drilling mud pressure during drilling, shrinkage of cement sheath due to cement hydration, the cyclic internal pressure and temperature during injection and production (Bu et al., 2020; Feng et al., 2017; Glover et al., 2016; Lin et al., 2020; Xi et al., 2018).

In addition, the formation and the cement sheath are porous mediums. There are a large number of pores and cracks in the natural rock mass. These defects not only change the mechanical properties of the rock mass, but also seriously affect the permeability characteristics and thermodynamic properties. The cement sheath and formation integrity are affected by the geological environment, that is, the hydrological field, mechanical field and thermal field. Generally, the thermal effect and fluid pore pressure act on the rock, leading to rock deformation. The deformation of the rock and fluid seepage lead to the redistribution of the temperature field. The rock deformation and the thermal effect lead to the change of the permeability characteristics and the pore fluid pressure of the formation, thus affecting the fluid seepage. It is important to note that the above three effects do not occur in isolation, but simultaneously. Therefore, the cement sheath integrity analysis needs to consider the influence of thermal–hydrological–mechanical (THM) coupling. Specially, during the injection/fracturing process, the ultrahigh-pressure and low-temperature fracturing fluid induce the severe variation of mechanical field, thermal field and hydrological field, in the meantime. However, most of the cement sheath integrity studies (Bois et al., 2011; De Andrade and Sangesland, 2016; Philippacopoulos and Berndt, 2002; Thiercelin et al., 1998; Zhang and Wang, 2017) only coupled thermal–mechanical or coupled hydrological–mechanical.

The cement sheath failure mechanism subjected to these factors (e.g., stress, temperature, pressure) has been extensively

* Corresponding author.
E-mail address: xiaorongli@cup.edu.cn (X.-R. Li).

https://doi.org/10.1016/j.petsci.2022.09.001
1995-8226/

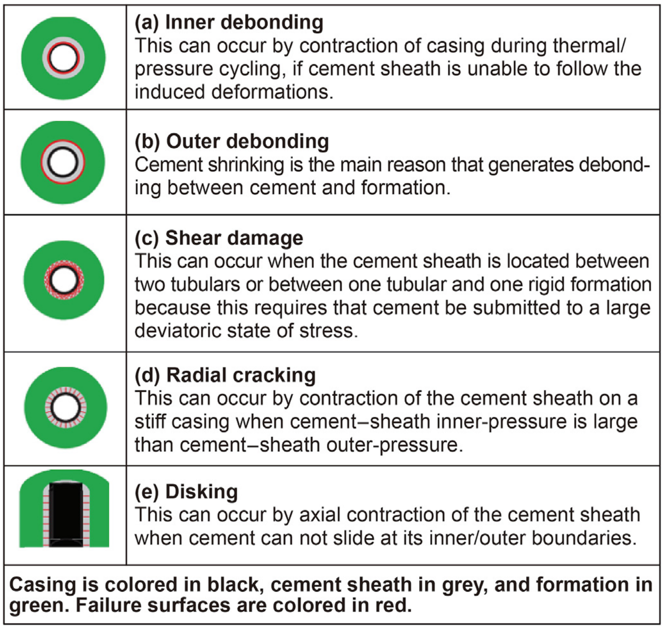

Fig. 1. Cement sheath damage (modified after Bois et al., 2012).

investigated. Yin et al. (2019) conducted a combined experimental and numerical studies to analyze the wellbore deformation subjected to thermal cycling loadings. The results indicated that some radial cracks are likely to occur due to the thermal expansion in a heating stage, while some cement debonding can be induced by the thermal contraction during a cooling stage. Besides, a contact resistance was introduced in the model to make the thermal diffusion more realistic compared to the experimental work. Lin et al. (2020) presented an experimental study of cement sheath failure under temperature and pressure cycle loading. The anti-sealing performance of the casing–cement sheath was measured under various loading–unloading methods. Other existing studies (De Andrade and Sangesland, 2016; Kuanhai et al., 2020) have also analyzed the cement sheath failure induced by thermal and pressure effects.

However, the loss of cement sheath integrity is a full life cycle failure problem under a complex loading history during drilling, casing, cementing, hardening, production, and injection. Many previous simulation studies (Medeiros de Souza et al., 2018; Shan et al., 2018; Therond et al., 2017) only concentrate on a particular stage of life-of-well without considering the loading history. The problem is that the initial stress state and strain or damage conditions at this particular stage are not clearly known. The plastic deformation will accumulate when plastic deformation occurs in the previous stages. It is difficult to get the accumulated plastic strain or damages without modeling the previous stages.

Besides, an initial stress state can be produced in the solid cement sheath at the end of the hardening process. As the cement slurry changes from the fluid to the solid porous framework, effective stress and pore pressure are generated, and the cement adheres to the casing and the formation. Eventually the cement sheath becomes an ideal impermeable barrier with the initial stress generated. However, the effects of this initial cement strength on cement sheath integrity are rarely considered in the existing numerical simulations of cement sheath integrity.

Therefore, this paper aims to develop a staged FEM model to simulate cement sheath integrity during life-of-well considering the non-linear interaction between casing/formation and the loading history of the system. The staged approach, based on a sophisticated THM coupling method, captures the development of stress and strain in the well system during all major stages. Especially, the initial stresses generated in the cement sheath after hardening has been incorporated in the model. The approach can monitor the development of the cement sheath debonding over the entire life-of-well.

2. Typical operation stages during life of well

The well system experiences different stress and deformation in different stages during the life of the well. It is essential to model each stage to obtain correct stress state and state variables (e.g., plasticity, damage, debonding) at the end of each stage. These stress state and state variables are then applied as initial conditions for modeling the next stage. Here we review the typical operational stages during the life of the well and the corresponding loading and boundary conditions.

Virgin state stage. No wellbore is created in the virgin state. Formation in this unperturbed state is generally subject to three orthogonal principal *in-situ* stresses, including overburden stress and two lateral stresses. The two lateral stresses, in the most general case, are not equal to each other.

Drilling stage. A cylindrical volume of rock is drilled out of the formation during this stage. At the same time, drilling mud is used to occupy the volume (Li et al., 2019a, 2019b; Mackay and Fontoura, 2014). As a result, the force exerted by the cylindrical rock on the surrounding formation is replaced by the hydrostatic pressure of the mud. This pressure replacement is usually capable of achieving “wellbore stability” by carefully designing the density of drilling mud (Li et al., 2019c). However, it is very difficult to duplicate the original stress equilibrium in the formation because the hydrostatic mud pressure is generally not equal to the original force in the removed rock. Moreover, for the most general case with unequal lateral stresses, it is impossible to maintain the original equilibrium. The formation around the wellbore has to deform, inducing local stress concentration.

Casing stage. During this stage, the steel casing is run into the borehole created in the drilling stage. The near-wellbore stress state usually does not have obvious change during this stage, unless considerable fluctuation to the mud pressure in the wellbore is induced by casing insertion. Hydrostatic mud pressure is exerted on both sides of the casing. Casing eccentricity may be introduced in this stage because of the general difficulty to align the casing to the axis of a borehole of a few thousand meters. However, in this study, the influence of casing eccentricity on cement sheath integrity is not considered. All the results reported in the following sections assume perfect casing centralization.

Cementing stage. During this stage, the cement slurry is added to the annulus. Hydrostatic mud pressure in the annulus is then replaced by the hydrostatic pressure of cement slurry, which acts on the outer surface of the casing and the wall of the formation. The pressure inside the casing might remain the same as the hydrostatic mud pressure. The change of fluid pressure inside the wellbore in this stage leads to further changes of stress and strain in the casing and surrounding formation.

Cement slurry hardening stage. After pouring cement slurry into the annulus, a certain period, depending on the specifications of the slurry, is required to allow cement hardening. The slurry gradually becomes solid cement to adhere with casing and formation as an impermeable barrier (Zhang and Eckert, 2020), which results in an initial stress state of cement sheath. Typically, this process is associated with volume shrinkage if there is no enough bloating agent in the cement slurry. Cement shrinkage can lead to the deformation of the casing, cement, and formation rock, which might cause the failure of cement bonding. Besides, the initial stress affects the magnitude of interface contact pressure, and further changes the stress distribution around the wellbore.

Completion stage. In the completion stage, the mud inside the casing is replaced by completion fluid, which in many cases has a relatively lower density. The resulting low pressure leads to additional deformation and might cause debonding.

Production stage. The pressure in the wellbore is further lowered during this stage to generate a pressure gradient from the formation to the wellbore, facilitating hydrocarbon production. The pressure exerting on the casing wall at this stage is generally lower than that experienced during any of the previous stages. Low casing pressure leads to displacement towards the center of the wellbore and reduces compressive radial stress at the cement interfaces, which may eventually result in debonding if the radial stress at the interface becomes tensile and overcomes the tensile strength of the bond. Typically, the production of reservoir fluid will heat the wellbore to some extent. This thermal effect will lead to an expansion of the wellbore components and lessen the risk of debonding.

Injection stage. It is a common practice to turn a production well into an injection well at some time point to enhance overall hydrocarbon recovery by waterflooding or to achieve some other objectives, such as gas storage, water disposal, and geothermal applications. The mechanical effect of fluid injection is quite similar to that of production but in the opposite way. High casing pressure associated with fluid injection leads to outward deformation and might heal debonding generated during previous stages of life-of-well. The injection fluid usually has a lower temperature compared with the *in-situ* temperature of a wellbore. As a result, the wellbore system will be cooled off to some extent during the injection stage. This cooling effect causes wellbore shrinkage and increases the likelihood of debonding.

3. Numerical approach

3.1. Model geometry

The staged well integrity model is developed, using the finite element platform Abaqus. As shown in Fig. 2, the three-dimensional model including three major components, i.e., casing, cement, and formation. The entire model size is 2 m × 2 m × 0.1 m; the cement sheath outer diameter is 0.3112 m (12.25 in); the casing outer diameter is 0.2508 m (9.875 in); and the casing inner diameter is 0.2168 m (8.539 in).

Coupled pore pressure and displacement element (C3D8P) in Abaqus are used to mesh the formation and the cement. This means the cement is also considered as a porous material in this study. The casing is considered as a linear elastic material and discretized with element C3D8. The interfaces between cement and casing and the interface between cement and formation are modeled using the pore pressure cohesive element COH3D8P with zero initial thickness.

In this paper, a sequential coupling approach is used to realize the THM coupling analysis process of the cement sheath. Fig. 3 is the flow chart of THM coupling model. Firstly, considering the heat transfer properties of the material, a casing/cement sheath/formation heat transfer model is established, and the thermal boundary conditions are applied to the model. The model temperature distribution at different stages is calculated. Then, considering the effects of mechanical properties and seepage properties, a hydrological-mechanical coupling casing/cement sheath/formation model is established, and the temperature distribution calculated in the heat transfer model is imported into the HM model. At the same time, the corresponding boundary conditions and load conditions are added to the model. Finally, quantitatively analyze the stress distribution and state variables of the cement sheath at different stages, e.g., plastic strain, damage, and debonding at cement/formation or cement/casing interface.

3.2. Material models

The casing is considered as an isotropic linear elastic material that obeys the generalized Hooke's law. Young's modulus and Poisson's ratio of the casing are 200 GPa and 0.3, respectively.

The cement sheath and formation are modeled as poro-elastoplastic materials and the plastic behavior defined by Mohr-Coulomb criterion:

$$H_{\mathrm{m}}q - p\tan\phi - C = 0 \tag{1}$$

with

$$H_{\mathrm{m}} = -\frac{1}{\sqrt{3}\cos\phi}\sin\left(\Theta+\frac{\pi}{3}\right)+\frac{1}{3}\cos\left(\Theta+\frac{\pi}{3}\right)\tan\phi \tag{2}$$

where ϕ is the friction angle of cement sheath and formation rock; C is the cohesion of cement sheath and formation rock; p is the equivalent pressure stress; q is the equivalent Mises stress.

$$p=\frac{1}{3}trace(\sigma) \tag{3}$$

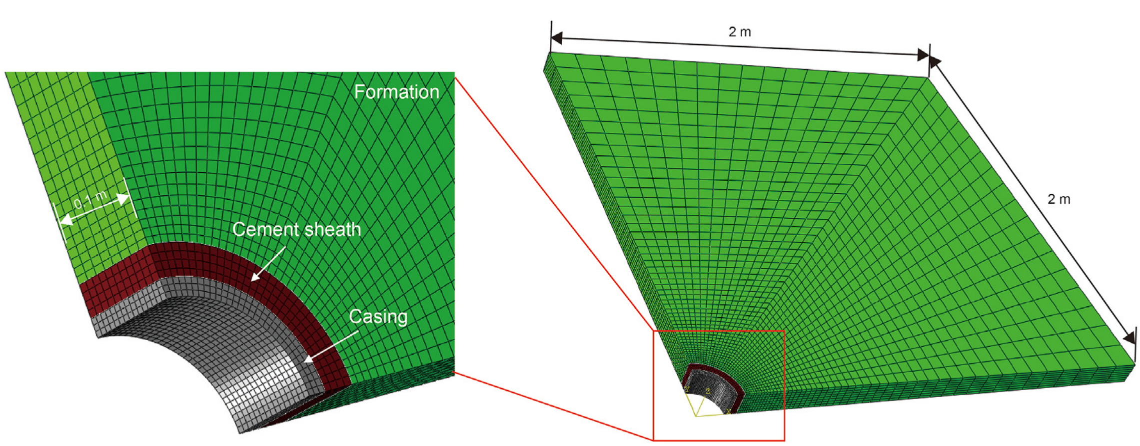

Fig. 2. The geometry and mesh of the cement sheath model.

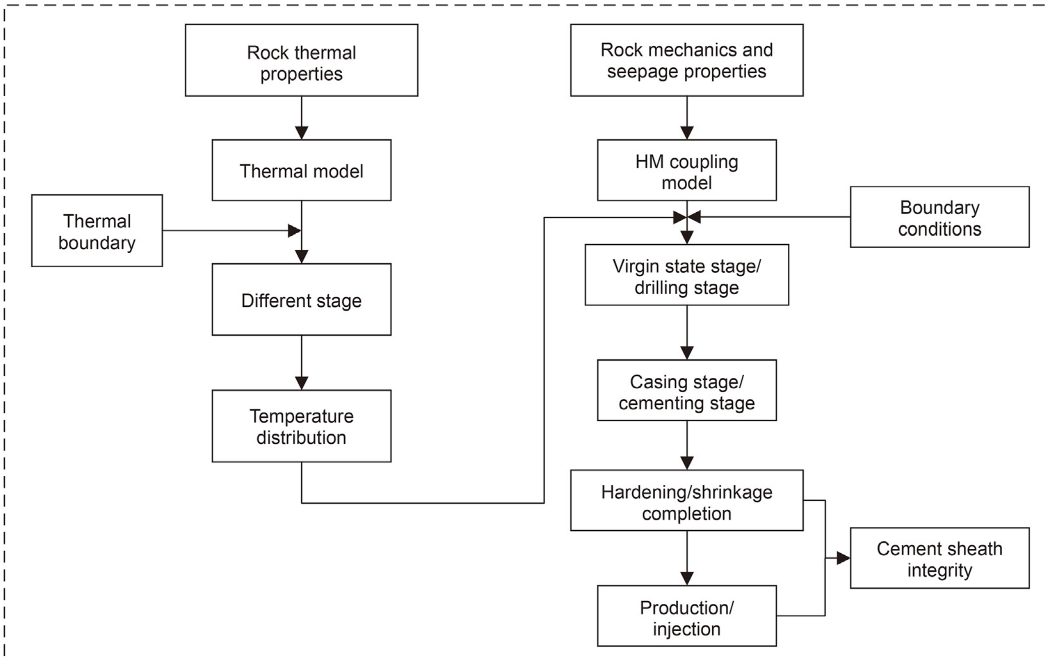

Fig. 3. Flow chart of THM coupling model.

$$q = \sqrt{\frac{3}{2}(S:S)} \tag{4}$$

Θ in Eq. (2) is the deviator polar angle, defined as:

$$\cos(3\Theta) = \left(\frac{g}{q}\right)^3 \tag{5}$$

g is the third invariant of deviatoric stress, defined as:

$$g = \left(\frac{9}{2}S \cdot S:S\right)^{\frac{1}{3}} \tag{6}$$

S is the deviatoric stress:

$$S = \sigma + pI \tag{7}$$

where σ is the total stress tensor; I is the identity matrix.

The fluid flow in the cement sheath and formation is assumed to obey Darcy' law:

$$q_\mathrm{i} = -\frac{k}{\mu}p_\mathrm{p} \tag{8}$$

where q_i is the fluid flux; k is the permeability of the porous medium; μ is the viscosity of the pore fluid; p_p is the pore pressure.

To account for thermal diffusion caused by the temperature difference between the wellbore and the formation, a series of thermal properties of the materials, including thermal expansion coefficient, specific heat, and thermal conductivity, are defined in this simulation. Assuming constant material properties during thermal diffusion, the governing equation of heat conduction can be expressed as:

$$\frac{\rho c}{\lambda}\frac{\partial T}{\partial t} = \nabla^2 T \tag{9}$$

where ρ is the density of the material; c is the specific heat capacity of the material; λ is the heat conductivity of the material; T is the temperature.

And the thermal strain can be expressed as:

$$\varepsilon_\mathrm{T} = -\alpha_\mathrm{T}(T - T_0) \tag{10}$$

where α_T is the coefficient of linear thermal expansion; T_0 is the initial temperature.

Table 1 shows the base-case material properties of the casing, cement, and formation used for the modeling, including the thermal expansion and diffusion parameters. The material properties of the formation and cement sheath are compiled from data provided in Gray et al. (2009) and Yang (2017).

Interface debonding is the main focus of this study. In the hardening stage, the cement slurry becomes cement sheath through hydration reaction. At the same time, the cement sheath is bonded to the casing and the formation, forming two interfaces with a certain cohesive force. In the subsequent operation conditions, under the influence of temperature and pressure, the traction force at the cement interface would change. In the previous model of Gray et al. (2009), the 'Hard' contact model in Abaqus is used to simulate the debonding behavior of the cement interface. However, it cannot explicitly capture the bonding behavior of the interfaces. In this study, cement interface behavior is defined by the

Table 1
Material properties for the casing, cement, and formation (Gray et al., 2009; Yang, 2017).

Material	Casing	Cement	Rock
Density, kg/m^3	8000	2240	2240
Modulus, GPa	200	10	50
Poisson's, dimensionless	0.3	0.25	0.3
Permeability, mD	–	0.001	0.1
Friction angle, degree	–	27	30
Cohesion, MPa	–	10	20
Thermal expansion coefficient, m/m/K	1.2e-5	1e-5	0.79e-5
Specific heat, J/kg/K	450	1600	1000
Thermal conductivity, W/m/K	50	1	2.1

traction−separation law. As shown in Fig. 4, t_n^o is the normal critical tensile stress of the element, which is the tensile strength of the cohesive element; t_s^o and t_t^o are the critical stresses in the other two tangential directions; δ_n^o is the normal nominal separation at damage initiation; δ_s^o and δ_t^o are the separations in the first shear and second shear directions at damage initiation, respectively; δ_n^f is the normal nominal separation at complete failure; δ_s^f and δ_t^f are the separations in the first shear and second shear directions at complete failure respectively. When the traction at the interface reaches the bond strength, the strength of the interface begins to degrade with further separation. Eventually, when the separation reaches a certain value, the traction decreases to zero and the interface opens completely. The area of the triangle in Fig. 4 is the fracture energy required to open the interface. The cohesive interface model can better describe the bonding/debonding behavior of the cement interface, but it needs more parameters compared with the 'Hard' contact model. In this study, we used the cohesive parameters reported in Table 2 as the base-case input parameters for casing/cement and cement/formation interfaces.

3.3. Modeling stages

In this section, we briefly describe the different steps in the simulation, which are corresponding to the different operational stages during the life of a well described in Section 2.

Step 1 **Initial equilibrium:** The first step is an initial equilibrium calculation. In this step, there is no wellbore. Virginal pore pressure and *in-situ* stress are applied to the model. By doing this, an initial stress equilibrium state can be obtained before doing any subsequent operations to the formation.

Step 2 **Drilling:** The second step is drilling. In this step, the wellbore elements are removed to create the borehole. In the meanwhile, the drilling mud pressure is applied to the surface of the wellbore wall. As a result, the stress concentration and associated deformation around the wellbore are obtained.

Step 3 **Casing:** Following the drilling step is the casing step. In this step, the casing elements are activated and the hydrostatic pressure of the drilling fluid is exerted on the inner and outer casing surfaces.

Step 4 **Cementing:** The cementing stage is a key process after the casing is run into the well. Its function is to seal the annular space between the casing and the wellbore to isolate the oil, gas, and water layers and to support the casing. The maximum pressure that the cement slurry can withstand in the annulus is at the end of the mud replacement, which is the sum of maximum hydrostatic pressure in the annulus and the annulus flow resistance. Hydrostatic mud pressure in the annulus is replaced by the hydrostatic pressure of cement slurry, which acts on the outer surface of the casing and the wall of the formation. The change of fluid pressure inside the wellbore in this stage leads to further changes of stress and strain in the casing and surrounding formation.

Step 5 **Hardening/shrinkage:** For simulation convenience, cement hardening and shrinkage are simulated as two separate steps. To model hardening process, the elements representing the cement are introduced with zero displacements, but with an initial uniform compressive stress state equal to the hydrostatic pressure of the cement slurry (Gray et al., 2009). When introducing cement elements, contacts between casing and cement, and cement and formation, are created at the same time. Previous hydrostatic pressures applied on the casing outer surface and wellbore surface are removed. During cement shrinkage, a volume reduction to the cement elements is applied gradually to represent cement shrinkage. This volume shrinkage might cause debonding of the interfaces defined in the previous step. Meanwhile, to consider the effects of the initial stress generated in cement sheath during hardening, a series of effective stress and pore pressure are applied in the modeling.

Step 6 **Completion:** During this step, the hydrostatic pressure of the completion fluid is applied to the inner surface of the casing. The previous mud pressure on the surface is removed.

Step 7 **Production:** The hydrostatic pressure of the completion fluid applied on the inner casing surface is replaced by a lower production pressure in this step. When considering thermal loading, a temperature boundary condition is applied on the inner casing surface.

Step 8 **Injection:** High injection pressure is applied on the inner surface of the casing. The previous production pressure is removed. The temperature boundary condition at the inner casing surface is activated when considering the thermal effect.

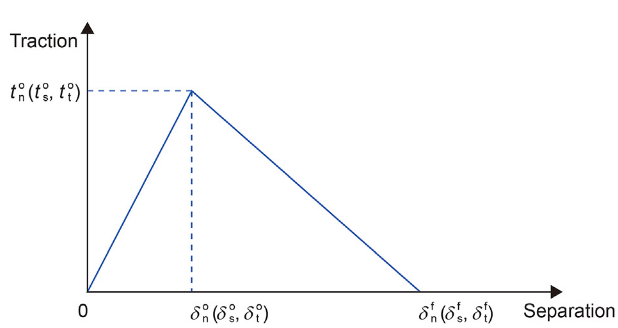

Fig. 4. Typical traction−separation response.

As mentioned previously, using this staged modeling approach, the stress, deformation, and failure of the system at the end of each stage of the well can be observed, and obtain the correct initial stress state and state variables such as plasticity, damage, debonding. Otherwise, the initial conditions are usually very difficult to be determined if only modeling a single, particular stage. In the following sections, some simulation results of the staged cement sheath integrity model are reported and analyzed.

3.4. Boundary and loading conditions

To simplify the model and improve the efficiency of calculation, a quarter model of the well system, including formation, casing, and cement, is developed for the simulation. In the initial condition before the drilling stage, the normal displacement is constrained on the outside of the model, symmetrical boundary conditions are applied on the cross section of the model, and the vertical displacement is constrained on the bottom surface. To avoid different axial strains due to different material properties in the formation, cement sheath, and casing, the vertical displacement of the upper surface is constrained, and the *in-situ* stress is applied by the predefined field. At the same time, the initial pore pressure and porosity are applied to the entire formation. During the casing step, the casing is activated, constraining the vertical displacement of the casing upper and bottom surfaces, and deploying symmetrical boundary conditions on the casing section. The cement sheath is activated during the hardening step, constraining the vertical

Table 2
Material properties for casing/cement and cement/formation interfaces (Wang and Taleghani, 2014).

Interface	Tensile bond strength, MPa	Shear bond strength, MPa	Cohesive stiffness, MPa	Fracture energy, J/m^2
Casing/cement interface	0.50	2.00	3e5	100
Cement/formation interface	0.42	0.42	3e5	100

displacement of the upper and bottom surfaces, and applying symmetrical boundary conditions at the cement sheath section. In the following steps, this mentioned boundary conditions and initial conditions keep constant.

During the thermal analysis, it is assumed that there is transit heat transfer between the casing, cement sheath, and the formation. The model has constant thermal properties during the simulation. The formation temperature is set to an initial temperature of 60 °C by the predefined field, and at the same time, a mandatory boundary condition with a temperature of 60 °C is set on the outside of the formation. The fluid temperature inside the casing in the high-temperature stage is 80 °C, and the fluid temperature inside the casing in the low-temperature stage is 15 °C.

The major loading conditions of each stage are as follows: In step 1, virginal pore pressure and *in-situ* stress are applied to the model. In step 2, the drilling mud pressure is applied to the surface of the wellbore wall. In step 3, the hydrostatic pressure of the drilling fluid is exerted on the inner and outer casing surfaces. In step 4, the hydrostatic pressure of cement slurry acts on the outer surface of the casing and the wall of the formation. In step 5, initial stress is added to the cement sheath. In step 6, the hydrostatic pressure of the completion fluid is applied to the casing inner surface.

$$K_{\mathrm{p}} = \frac{1+\sin\phi}{1-\sin\phi} \tag{12}$$

$$q = 2C\tan\left(45+\frac{\phi}{2}\right) \tag{13}$$

where r_{w} is the radius of the wellhole; P_0 is the uniform initial *in-situ* stress; P_{i} is the internal pressure; C is the cohesion of formation rock; ϕ is the friction angle of formation rock.

The stresses in the plastic zone are:

$$\sigma_r = -\frac{q}{K_{\mathrm{p}}-1} + \left(p_{\mathrm{i}}+\frac{q}{K_{\mathrm{p}}-1}\right)\left(\frac{r}{r_{\mathrm{w}}}\right)^{K_{\mathrm{p}}-1} \tag{14}$$

$$\sigma_\theta = -\frac{q}{K_{\mathrm{p}}-1} + K_{\mathrm{p}}\left(p_{\mathrm{i}}+\frac{q}{K_{\mathrm{p}}-1}\right)\left(\frac{r}{r_{\mathrm{w}}}\right)^{K_{\mathrm{p}}-1} \tag{15}$$

where r is the distance to the center of the wellhole; σ_r is the radial stress; σ_θ is the tangential stress.

The displacements in the plastic zone are:

$$u_r = \frac{r}{2G}\left[(2\nu-1)\left(p_0+\frac{q}{K_{\mathrm{p}}-1}\right) + \frac{(1-\nu)\left(K_{\mathrm{p}}^2-1\right)}{K_{\mathrm{p}}+K_{\mathrm{ps}}}\left(p_{\mathrm{i}}+\frac{q}{K_{\mathrm{p}}-1}\right)\left(\frac{R_0}{r_{\mathrm{w}}}\right)^{K_{\mathrm{p}}-1}\left(\frac{R_0}{r}\right)^{K_{\mathrm{ps}}+1} + \left(\frac{(1-\nu)\left(K_{\mathrm{p}}K_{\mathrm{ps}}+1\right)}{K_{\mathrm{p}}+K_{\mathrm{ps}}}-\nu\right)\left(p_{\mathrm{i}}+\frac{q}{K_{\mathrm{p}}-1}\right)\left(\frac{R_0}{r_{\mathrm{w}}}\right)^{K_{\mathrm{p}}-1}\right] \tag{16}$$

3.5. Model validation

3.5.1. Theoretical verification

To validate the accuracy of the proposed model, the stresses and displacements around the wellbore immediately after the drilling process are calculated from the numerical model and compared against the analytical solutions. In this scenario, the formation is assumed as an elastoplastic medium, and the associated governing equations of the analytical solution are shown in Eqs. (11)–(20). Uniform *in-situ* stress (P_0), zero wellbore pressure, and other detailed parameters as listed in Table 3 are applied in the calculation.

Based on the analytical poro-elastoplastic solution derived by Salencon (1969), the radius of the plastic zone, R_0, is given as (Salencon, 1969):

$$R_0 = r_{\mathrm{w}}\left(\frac{2}{K_{\mathrm{p}}+1}\,\frac{P_0+\frac{q}{K_{\mathrm{p}}-1}}{P_{\mathrm{i}}+\frac{q}{K_{\mathrm{p}}-1}}\right)^{1/(K_{\mathrm{p}}-1)} \tag{11}$$

$$K_{\mathrm{ps}} = \frac{1+\sin\varphi}{1-\sin\varphi} \tag{17}$$

where ν is the Poisson's ratio; φ is the dilation angle; G is the shear modulus.

The stresses and displacements in the elastic zone are:

Table 3
Parameters used in the elasto-plastic model (Salencon, 1969).

Parameter	Value
Young's modulus E, GPa	6.778
Shear modulus G, GPa	2.8
Poisson's ratio ν	0.21
Cohesion strength C	3.45
Friction angle ϕ, degree	30
Dilation angle φ, degree	30
In-situ stresses P_0, MPa	30
Wellbore pressure P_{i}, MPa	0
Wellbore radius a, m	0.1556

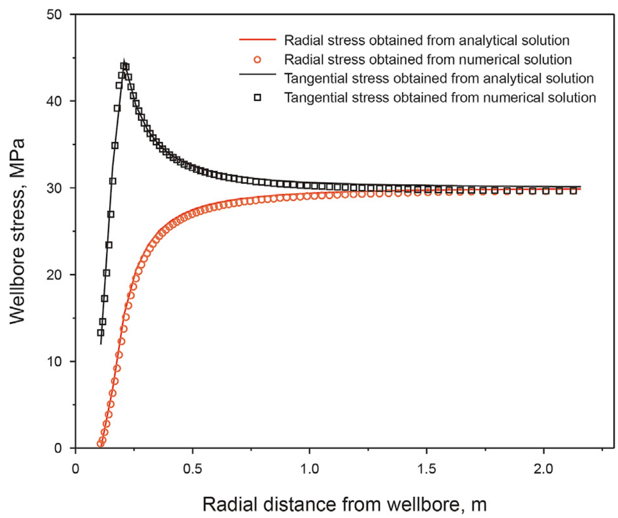

Fig. 5. Comparison of radial and tangential stresses along with the radial distance obtained from analytical solution and numerical model.

$$\sigma_r = P_0 - \left(P_0 - \frac{2P_0 - q}{K_p + 1}\right)\left(\frac{R_0}{r}\right)^2 \tag{18}$$

$$\sigma_\theta = P_0 + \left(P_0 - \frac{2P_0 - q}{K_p + 1}\right)\left(\frac{R_0}{r}\right)^2 \tag{19}$$

$$u_r = \frac{R_0^2}{2G}\left(P_0 - \frac{2P_0 - q}{K_p + 1}\right)\frac{1}{r} \tag{20}$$

Fig. 5 compares the radial and tangential stresses around the wellbore from the analytical solution and numerical model. Results show a good agreement. Also, we can get the same conclusion that the calculated results from the analytical solution and numerical model have a perfect agreement about the distribution of the radial displacement around the wellbore, as shown in Fig. 6. Therefore, the accuracy of the meshing and boundary conditions of this model can be proved.

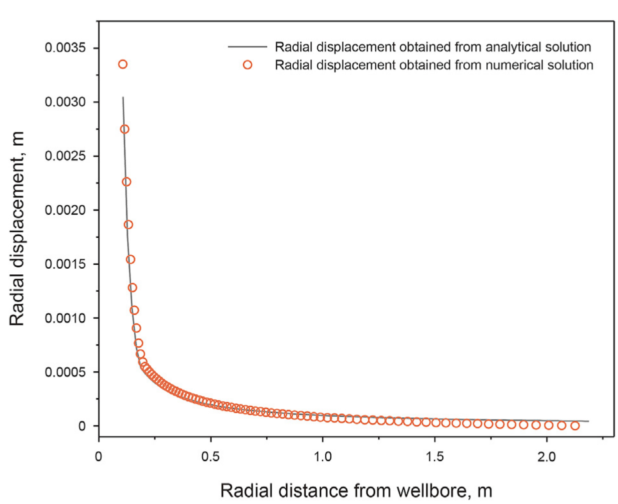

Fig. 6. Comparison of radial displacement along with the radial distance obtained from analytical solution and numerical model.

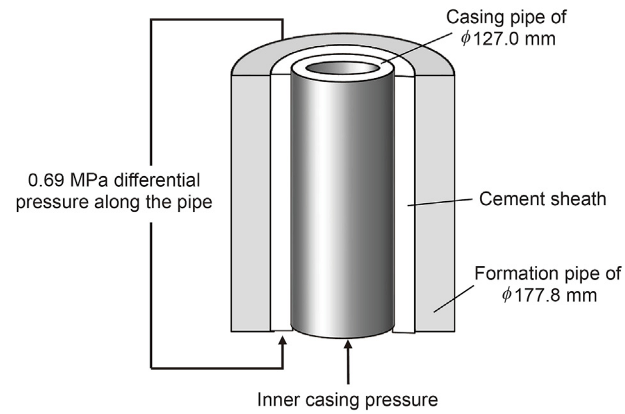

Fig. 7. The experiment setup of Jackson and Murphey (modified after Jackson and Murphey, 1993).

3.5.2. Experimental verification

Jackson and Murphey (1993) conducted a cement sheath integrity experiment under variable casing internal pressure. In this section, the numerical results are compared with Jackson and Murphey's experiments. The experimental setup consists of the inner casing, cement sheath and outer casing, which the outer casing is to replace the influence of the formation, as shown in Fig. 7. The experimental procedure includes three steps. Firstly, the class G cement slurry is poured into the annulus between the two casings, and fully cured at 48.9 °C and 6.9 MPa until the cement sheath is formed. Next, there is a pressure difference of 0.69 MPa between the top and bottom of the cement sheath. Finally, the internal pressure of the casing is loaded to 14, 28, 41, 55, and 69 MPa, and then gradually unloaded. Meanwhile, the degree of gas channeling under different internal pressures is detected. Using the numerical modeling method introduced in the previous section, a numerical model of inner casing-cement sheath-outer casing is established. The geometry and material parameters are referred to the experiment, as shown in Table 4.

Larger casing internal pressure can cause plastic deformation of the cement sheath. As the internal pressure of the casing decreases, the inner casing and the cement sheath continue to shrink inwards. Due to the inconsistent deformation, the cement sheath interface can generate tensile stress. When the tensile stress is bigger than the bonding strength of the interface, debonding will occur.

Fig. 8 shows the variation of the cement sheath debonding size with the unloading pressure under five different casing internal pressure schemes. The results indicate that when the casing internal pressure is loaded to 14, 28, and 41 MPa, no debonding occurs on the external surface of the cement sheath during the unloading process. During the unloading process from 55 to 0 MPa, the cement sheath debonding occurs when the pressure is 1.51 MPa, and the final debonding size is 2.82 μm. During the unloading process from 69 to 0 MPa, the cement sheath debonding occurs when the pressure is 3.45 MPa, and the final debonding size

Table 4
The parameters of Jackson and Murphey's experiment (Jackson and Murphey, 1993).

Material	Inner casing	Cement	Outer casing
Inner diameter, mm	108.6	127	154.78
Outer diameter, mm	127	154.78	177.8
Young's modulus, GPa	210	13.8	210
Poisson's ratio	0.3	0.25	0.3
Friction angle, degree	–	30	–
Cohesion, MPa	–	5.77	–

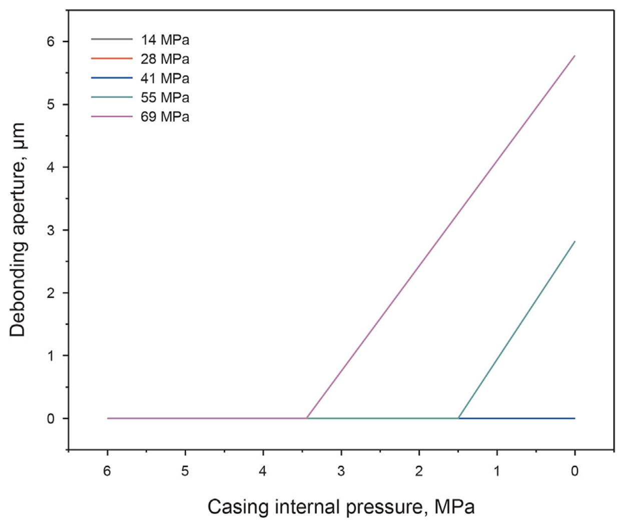

Fig. 8. Debonding size with the unloading pressure under five casing internal pressure schemes.

is 5.78 μm. The experimental results of Jackson and Murphey showed that the highest internal pressure of the casing was 14, 28, and 41 MPa, and no gas channeling was detected. When the casing internal pressure was loaded to 55 and 69 MPa, and then unloaded to 1.4 and 3.3 MPa, respectively, obvious gas channeling was detected. The numerical calculation results are consistent with the experimental results, proving the accuracy of the numerical model.

4. Results and discussion

4.1. Cement sheath integrity during life-of-well

Fig. 9 is a series of snapshots of the model during the simulation, showing the behavior of the casing–cement–formation system in different stages. At the beginning initial equilibrium stage, there is no wellbore. In the drilling stage, the wellbore is created and the wellbore wall moves inward because the drilling fluid pressure is smaller than the *in-situ* stress. Casing elements are added in the casing stage. In the cementing stage, the drilling fluid pressure in the annulus is replaced with the cement slurry pressure. Because the latter is larger, the casing moves inward while the wellbore wall moves outward. During hardening, the cement slurry solidifies to a cement sheath, and its volume shrinks, resulting in debonding at the cement/formation interface. The casing pressure decreases during completion and production, the debonding size becomes larger. During injection, due to the increased casing pressure, the debonding tries to heal.

4.1.1. Stress

The plots in Fig. 10 show the evolution of hoop stress in the formation around the wellbore after different stages. Tension is defined as positive stress and compression is defined as negative stress in this study. The results indicate that replacing drilling fluid pressure with cement slurry pressure in the cementing stage results in less compressive hoop stress in the formation around the wellbore. Cement hardening creates more compressive hoop stress. After hardening, changing in casing pressure has a very small effect on formation stress.

Fig. 11 shows the evolution of hoop stress in the outer side of cement sheath, which can be used as an indicator to evaluate the risk of the tensile radial crack in the cement. The initial stress state in the cement is compressive. After hardening, due to cement shrinkage and debonding of cement/formation interface, hoop stress in cement becomes tensile. The maximum tension is at the outer cement surface (if there is no debonding, the maximum tensile stress will be at the inner cement surface). The results show that decreasing casing pressure (during production) will decrease tensile hoop stress, and increasing casing pressure (during injection) will increase hoop stress, thereby increasing the risk of radial fractures.

Fig. 12 shows the evolution of the radial stress in the cement sheath, which can be used as an indicator to assess the risk of debonding at the cement sheath interface. The results show the stress state on the outside of the cement sheath is tensile, and the stress state on the inside of the cement sheath is compressive. In the hardening stage, the cement slurry undergoes a hydration reaction, the volume of the cement sheath continues to decrease, and the outer side of the cement sheath keeps shrinking inward. In the initial stage of hardening, the outer side of the cement sheath has

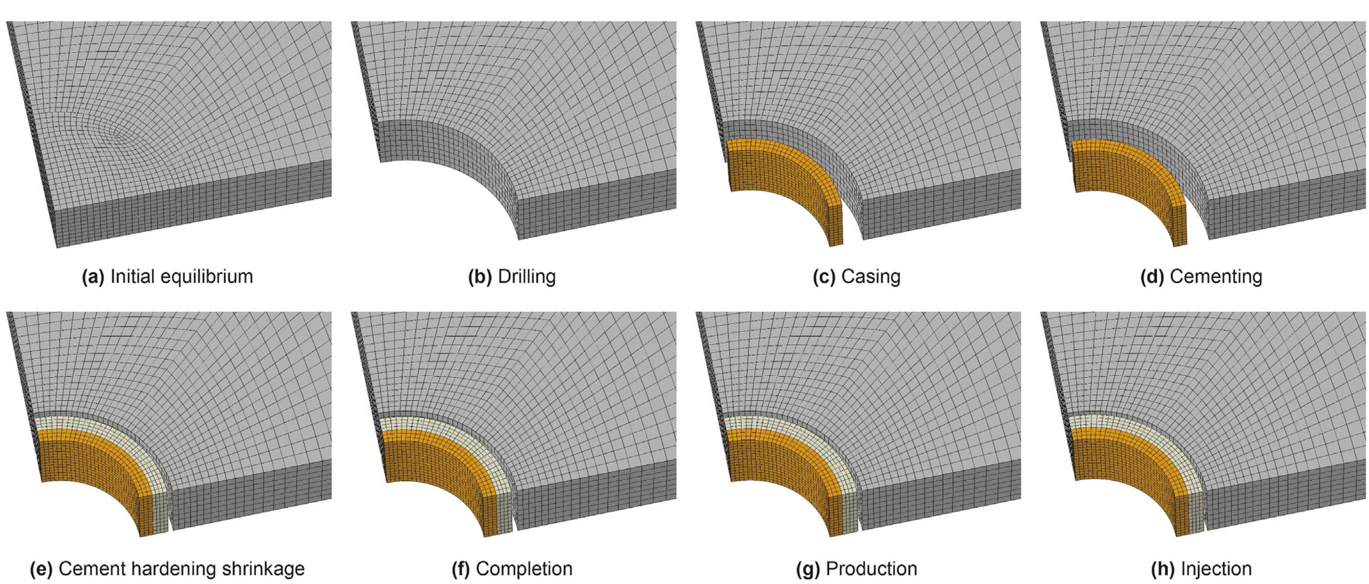

Fig. 9. Snapshots of each simulation step.

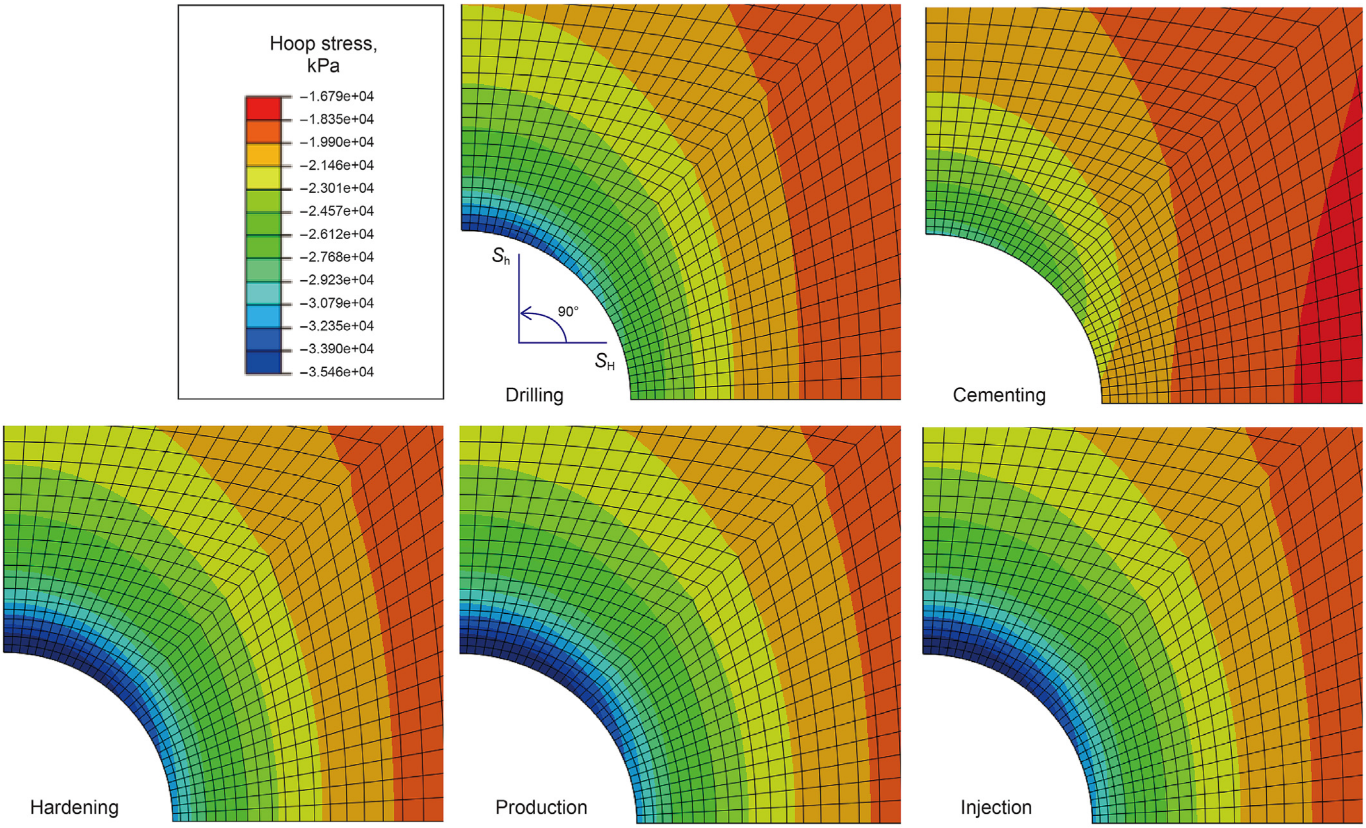

Fig. 10. Hoop stress in the formation at different stages.

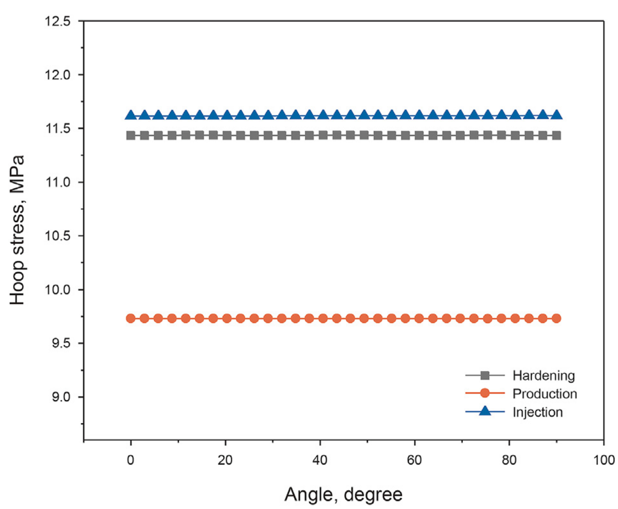

Fig. 11. Hoop stress on the outer side of cement sheath at different stages.

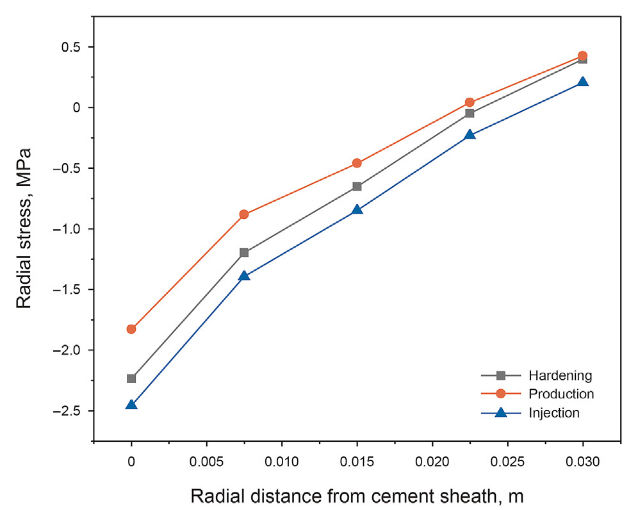

Fig. 12. Radial stress in the cement sheath at different stages.

inward compressive stress. When the stress exceeds the interface cohesive force, micro-annulus appears at the interface, and the outer side of the cement sheath would become tensile stress. In the production stage, the pressure inside the casing decreases, and the compressive stress inside the cement sheath decreases, which reduces the support for the cement sheath and increases the interface debonding size. In the injection stage, the internal pressure of the casing increases, and the compressive stress inside the cement sheath increases, reducing the debonding size. The results indicate that a higher casing pressure can reduce the risk of debonding at the cement sheath interface.

4.1.2. Plastic strain

Fig. 13 is the contour plots showing the plastic strain in the cement after the hardening, production, and injection stages. The equivalent plastic strain is a measure of the plastic deformation of a material, and its physical meaning is a quantity that represents the cumulative value of plastic strain proposed to record the history of deformation. In this work, the PEEQ is defined by $\varepsilon^{pl} = \int \frac{1}{c}\boldsymbol{\sigma} : \mathrm{d}\boldsymbol{\varepsilon}^{pl}$,

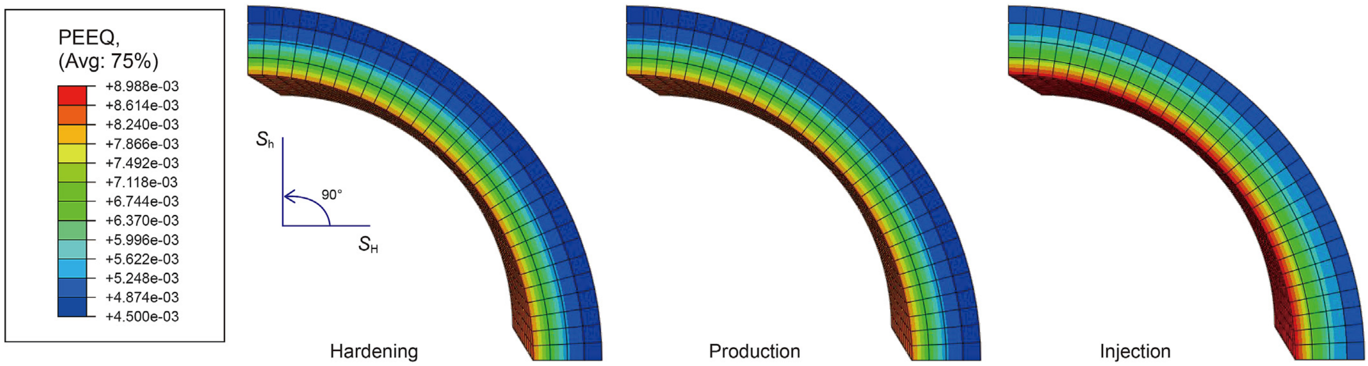

Fig. 13. Equivalent plastic strain (PEEQ) in the cement sheath at different stages.

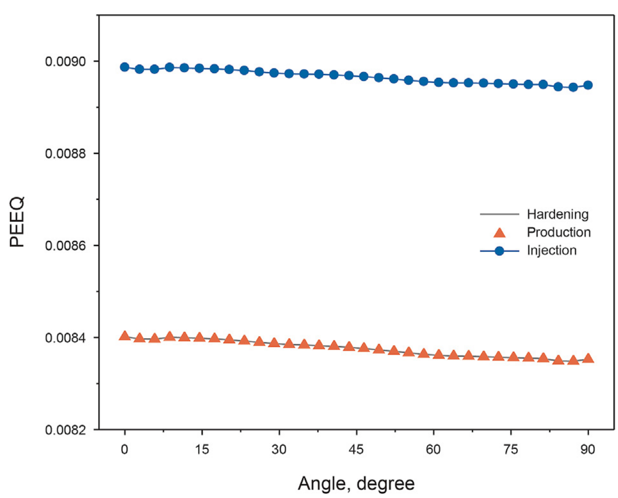

Fig. 14. PEEQ along with cement inner surface (angle 0° at the direction of S_H and 90° at the direction of S_h).

where *c* is the cohesion yield stress (SIMULIA, 2017). The equivalent plastic strain (PEEQ) can be used as an indicator of plastic damage to the cement. Fig. 14 shows the PEEQ along the cement inner surface with an angle of 0° at the direction of S_H and 90° in the direction of S_h. As shown in Fig. 14, the maximum plastic strain occurs at the inner surface of the cement sheath. Comparing the equivalent plastic strain after each stage, it can be seen that production (or decreasing the casing pressure) does not induce additional plastic strain in this case. However, the injection does increase the plastic strain in the cement and thus the risk of plastic failure.

4.1.3. Cement interface debonding

Cement debonding is the main focus of this study. Fig. 15 shows the interface debonding after cement shrinkage. In this study, only cement/rock interface debonding is observed. This is consistent with many other studies that show that the debonding is more likely to occur at the cement/formation interface. This is possible because the radial compressive stress is usually much larger at the casing/cement interface than that at the cement/formation interface due to stress concentration.

Fig. 16 shows the debonding at the cement/formation interface around the wellbore at the end of different stages. The angle is 0° in the direction of S_H and 90° in the direction of S_h. It can be seen that debonding is larger in the direction of S_h because there is less resistance for crack opening. The results also show that the debonding aperture increases after production due to decreased casing pressure and decreases after injection due to increased casing pressure. This example shows the capabilities of the model in predicting the stress and plastic damage of the cement, as well as the cement interface debonding. In the following parts, the results of a parametric study will be presented to investigate the effects of cement shrinkage, cyclic casing pressure, cyclic thermal stress, and the cement sheath initial stress on the integrity of the cement

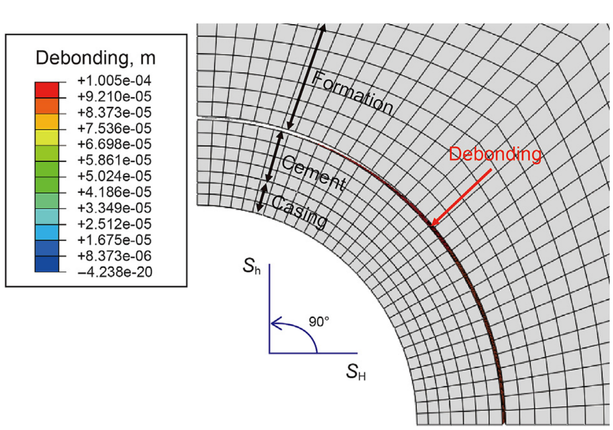

Fig. 15. Interface debonding after cement shrinkage.

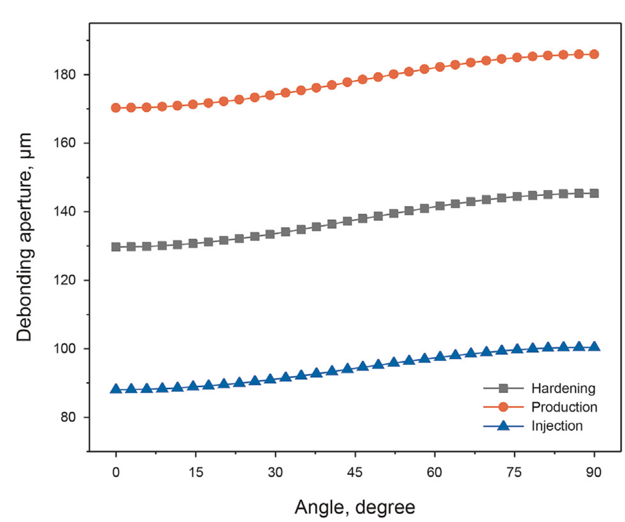

Fig. 16. Debonding along with cement/formation interface.

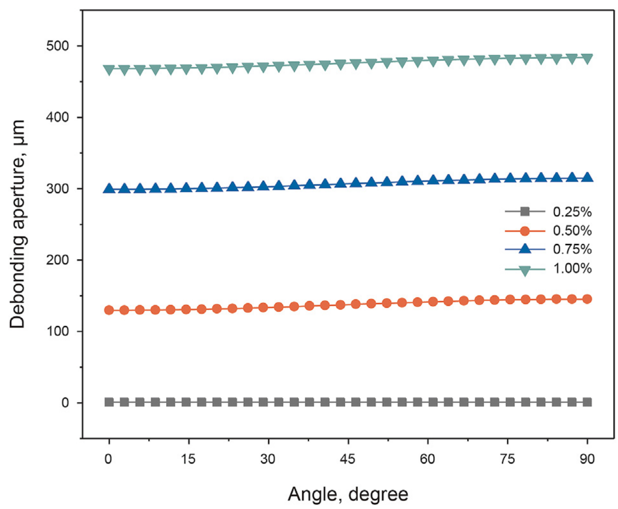

Fig. 17. Debonding for different cement shrinkage percentages after hardening.

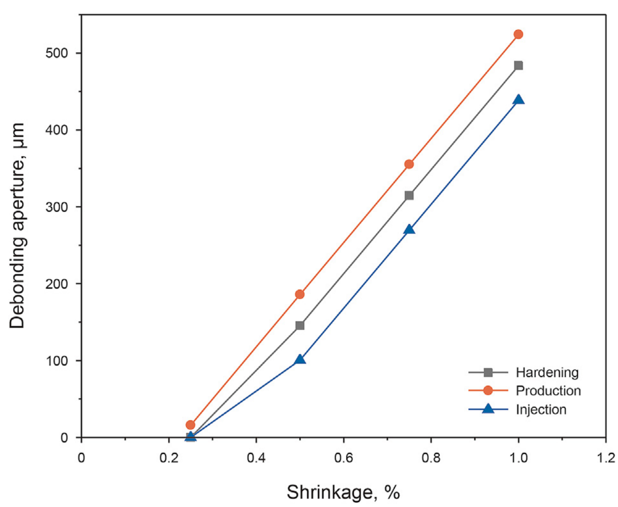

Fig. 18. Debonding at the S_h direction for different cement shrinkage percentages after different stages.

sheath, with the main focus on cement interface debonding.

4.2. Influence of cement sheath shrinkage

Fig. 17 shows the influence of cement shrinkage on cement/formation interface debonding aperture around the wellbore. The result indicates that debonding is very sensitive to the percentage of cement shrinkage. An 0.25% increase in the shrinkage volume can result in an increase of 150 μm in debonding aperture in this case. Again, the maximum debonding is along with the S_h direction. Fig. 18 shows the debonding at the S_h direction for different cement shrinkage percentages after different stages. The results show that the debonding size increases with the increase in cement shrinkage. When the cement shrinkage rate is 1%, the interfacial debonding sizes in the hardening, production and injection stages are 483.73, 524.26, and 438.63 μm, respectively.

4.3. Influence of cyclic casing pressure

In the process of production and injection of a well, the inside casing surface is subjected to alternating pressure, which may

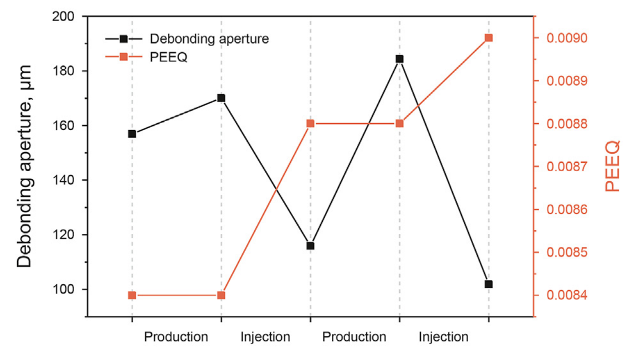

Fig. 19. Evolution of debonding and equivalent plastic strain with cyclical casing pressure (production with casing pressure 10 MPa – injection with casing pressure 40 MPa – production with casing pressure 5 MPa – injection with casing pressure 45 MPa).

cause the failure of the cement sheath. The cement sheath behavior is modeled with cyclical casing pressure, including pressure decrease in the production stage and pressure buildup in the injection stage. The whole loading process includes production with casing pressure 10 MPa, injection with casing pressure 40 MPa, production with casing pressure 5 MPa, and injection with casing pressure 45 MPa.

Fig. 19 quantifies the development of debonding and PEEQ during depressurizing the wellbore in the production stage and during pressurizing the wellbore in the injection stage. When the internal pressure of the casing increases from 10 to 40 MPa, the equivalent plastic strain of the cement sheath also increases, but the debonding aperture decreases from the original 170.04 to 115.94 μm. When the casing pressure is reduced from 40 to 5 MPa, the equivalent plastic strain of the cement sheath does not change, and the debonding aperture increases from the original 115.94 to 184.40 μm. Depressurizing the wellbore in production increases the debonding aperture but does not induce additional plastic strain. Pressurizing the wellbore in injection reduces the debonding but increases the plastic strain. The reason is that when the internal pressure of the casing increases, the supporting effect of the casing on the cement sheath is enhanced, resulting in the reduction of the debonding aperture.

4.4. Influence of cyclic thermal effect

The staged finite element model can also be used to investigate the periodic thermal effect on well integrity. Fig. 20 shows the

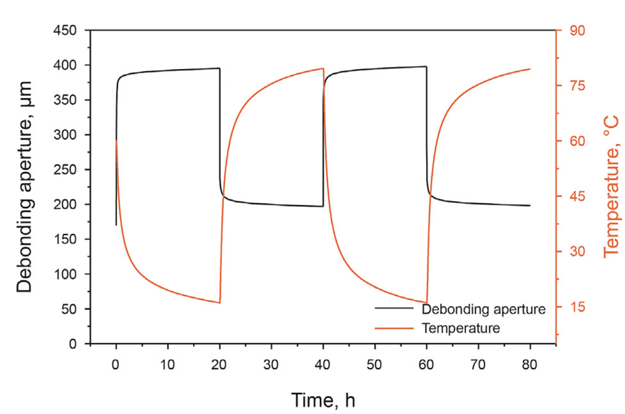

Fig. 20. Evolution of debonding at the cement/formation interface with cyclical temperature.

deboning and the temperature at the cement/formation interface. Both are a function of time because of the transient temperature diffusion. During cooling, debonding occurs at the cement/formation interface, the maximum debonding aperture is 397.88 μm, while during heating, the crack tends to heal, the debonding aperture is 169.64 μm. The reason for this phenomenon is that during the cooling process, the temperature gradually decreases, the volume of the cement sheath shrinks, and the cement sheath interface moves inward, so the debonding aperture increases. As the temperature rises, the volume of the cement sheath expands, so the debonding aperture decreases.

4.5. Influence of cement sheath initial stresses

The initial stresses of cement sheath represent how far the material is from the yield surface and, as a consequence, how much loading it can be submitted to before being damaged (Bois et al., 2008). It is crucial to reveal the effect of the initial stress of cement sheath on the integrity of the wellbore. As a result of the hydration reaction in the cement slurry, the water is gradually consumed and the pressure in the cement column decreases (Cooke et al., 1983; Sabins et al., 1982), but the cement gel strength increases with the cement hydration products accumulated gradually. However, there is still not a sufficient method to determine or detect the initial stress of cement sheath. In this paper, it is assumed that the hydrostatic pressure of cement slurry turns into the initial stress and pore pressure of cement sheath. The effects of cement sheath on interface debonding and PEEQ are analyzed.

Fig. 21 shows the influence of different initial stresses of the cement sheath on cement/formation interface debonding aperture around the wellbore. The results indicate that the initial stress of the cement sheath significantly affects the debonding of the cement sheath/formation interface. The debonding size of the interface decreases with the increase in the initial stress of the cement sheath. When the initial stress increases from 0 to 30 MPa, the maximum debonding size of the interface changes from 218.62 to 115.81 μm, with a decrease of 102.81 μm. The initial stress of the cement sheath is related to the curing time and the cement slurry system. Therefore, during the field application, the curing time of the cement slurry should be increased, or a short-setting cement slurry system should be selected to reduce the risk of debonding at the cement sheath interface.

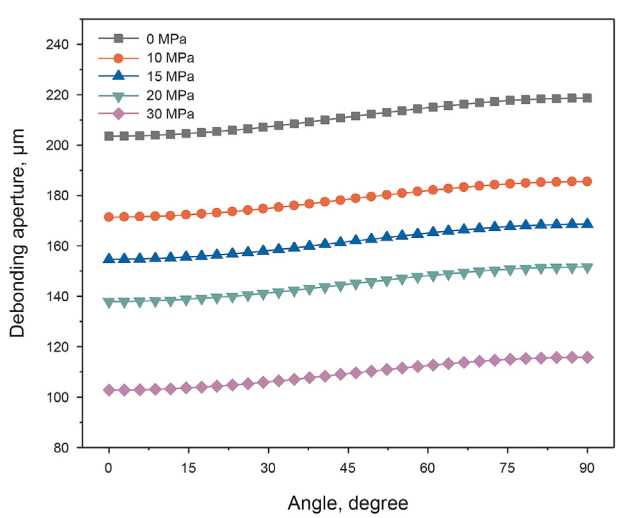

Fig. 21. Debonding size of cement/formation interface with different cement sheath initial stresses.

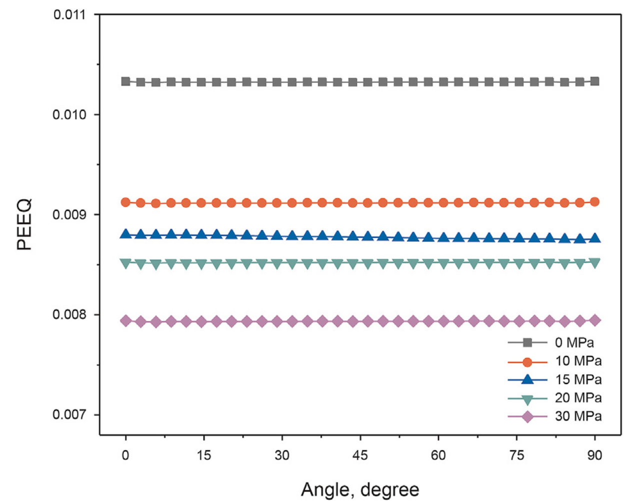

Fig. 22. The PEEQ of cement sheath with different initial stresses.

Fig. 22 shows the plastic strain of cement sheath with different initial stresses. The results show that the equivalent plastic strain of the cement sheath decreases with the increase in the initial stress of the cement sheath. It indicates that the initial stress can effectively reduce cement sheath plastic damage.

5. Conclusions

A staged finite-element modeling approach is proposed to simulate the behavior of casing–cement and cement–formation interfaces during life-of-well. This approach allows recording of stress and strain states during all well construction stages, and thus eliminates the guess of the initial state of each stage. The model quantifies cement sheath failure and debonding induced by cement shrinkage, cyclic casing pressure, wellbore temperature and initial stress of the cement sheath. The results show that cement sheath debonding is very sensitive to cement shrinkage during the cement hardening process, which can be further aggravated by casing pressure and temperature fluctuations during subsequential stages. Compared with the cyclic pressure, the debonding size of the cement sheath is more sensitive to temperature change. Meanwhile, the higher initial stress of the cement sheath can reduce the risk of interfacial debonding, as well as reduce the plastic damage of the cement sheath itself. The staged THM model developed in this paper quantifies multiple interacting physical components and processes during the life of a well. The simulation results confirm the need for modeling all well construction stages, taking cement sheath initial stress into account, and considering THM coupling for an accurate analysis of well integrity over the entire well life.

Acknowledgments

This work was financially supported by Science Foundation of China University of Petroleum, Beijing (No. 2462019BJRC011 and No. 2462020YXZZ051) and National Natural Science Foundation of China (No. 52004298).

References

Bois, A.-P., Saint-Marc, J., Garnier, A., 2008. Initial state of stress: the key to achieving long-term cement-sheath integrity. In: SPE Annual Technical Conference and Exhibition. Society of Petroleum Engineers. https://doi.org/10.2118/116651-MS.

Bois, A.-P., Garnier, A., Rodot, F., Saint-Marc, J., Aimard, N., 2011. How to prevent loss of zonal isolation through a comprehensive analysis of microannulus formation.

SPE Drill. Complet. 26, 13–31.
Bois, A.-P., Garnier, A., Galdiolo, G., Laudet, J.-B., 2012. Use of a mechanistic model to forecast cement-sheath integrity. SPE Drill. Complet. 27, 303–314. https://doi.org/10.2118/139668-PA.
Bu, Y., Ma, R., Guo, S., Du, J., Liu, H., Cao, X., 2020. A theoretical evaluation method for mechanical sealing integrity of cementing sheath. Appl. Math. Model. 84, 571–589. https://doi.org/10.1016/j.apm.2020.03.001.
Cooke, C.E., Kluck, M.P., Medrano, R., 1983. Field measurements of annular pressure and temperature during primary cementing. J. Petrol. Technol. 35, 1429–1438. https://doi.org/10.2118/11206-PA.
De Andrade, J., Sangesland, S., 2016. Cement sheath failure mechanisms: numerical estimates to design for long-term well integrity. J. Petrol. Sci. Eng. 147, 682–698. https://doi.org/10.1016/j.petrol.2016.08.032.
Feng, Y., Li, X., Gray, K.E., 2017. Development of a 3D numerical model for quantifying fluid-driven interface debonding of an injector well. Int. J. Greenh. Gas Control 62, 76–90. https://doi.org/10.1016/j.ijggc.2017.04.008.
Glover, K., Priolo, S., Heinricks, C., 2016. Risk-based analysis of thermal well integrity through integration of caprock geomechanics and cement sheath design. In: SPE Thermal Well Integrity and Design Symposium. Society of Petroleum Engineers. https://doi.org/10.2118/182510-MS.
Gray, K.E., Podnos, E., Becker, E., 2009. Finite-element studies of near-wellbore region during cementing operations: Part I. SPE Drill. Complet. 24, 127–136. https://doi.org/10.2118/106998-PA.
Jackson, P.B., Murphey, C.E., 1993. Effect of casing pressure on gas flow through a sheath of set cement. In: SPE/IADC Drilling Conference. Society of Petroleum Engineers ttps://doi.org/10.2118/25698-MS.
Kuanhai, D., Yue, Y., Yi, H., Zhonghui, L., Yuanhua, L., 2020. Experimental study on the integrity of casing-cement sheath in shale gas wells under pressure and temperature cycle loading. J. Petrol. Sci. Eng. 195, 107548. https://doi.org/10.1016/j.petrol.2020.107548.
Li, X., El Mohtar, C.S., Gray, K.E., 2019a. Modeling progressive breakouts in deviated wellbores. J. Petrol. Sci. Eng. 175, 905–918. https://doi.org/10.1016/j.petrol.2019.01.007.
Li, X., El Mohtar, C.S., Gray, K.E., 2019b. 3D poro-elasto-plastic modeling of breakouts in deviated wells. J. Petrol. Sci. Eng. 174, 913–920. https://doi.org/10.1016/j.petrol.2018.11.086.
Li, X., Feng, Y., El Mohtar, C.S., Gray, K.E., 2019c. Transient modeling of borehole breakouts: a coupled thermo-hydro-mechanical approach. J. Petrol. Sci. Eng. 172, 1014–1024. https://doi.org/10.1016/j.petrol.2018.09.008.
Lin, Y., Deng, K., Yi, H., Zeng, D., Tang, L., Wei, Q., 2020. Integrity tests of cement sheath for shale gas wells under strong alternating thermal loads. Nat. Gas. Ind. B 7 (6), 671–679. https://doi.org/10.1016/j.ngib.2020.05.006.
Mackay, F., Fontoura, S.A.B., 2014. The description of a process for numerical simulations in the casing cementing of petroleum salt wells – Part I: from drilling to cementing. In: 48th U.S. Rock Mechanics/Geomechanics Symposium. American Rock Mechanics Association.
Medeiros de Souza, W.R., Bouaanani, N., Martinelli, A.E., Bezerra, U.T., 2018. Numerical simulation of the thermomechanical behavior of cement sheath in wells subjected to steam injection. J. Petrol. Sci. Eng. 167, 664–673. https://doi.org/10.1016/j.petrol.2018.04.023.
Philippacopoulos, A.J., Berndt, M.L., 2002. Mechanical response and characterization of well cements. In: SPE Annual Technical Conference and Exhibition. Society of Petroleum Engineers. https://doi.org/10.2118/77755-MS.
Sabins, F.L., Tinsley, J.M., Sutton, D.L., 1982. Transition time of cement slurries between the fluid and set states. Soc. Petrol. Eng. J. 22 (6), 875–882. https://doi.org/10.2118/9285-PA.
Salencon, J., 1969. Contraction Quasi- Statique D'une Cavite a Symetrie Spherique Ou Cylindrique Dans Un Milieu Elasto-Plastique [WWW Document]. undefined. URL/paper/CONTRACTION-QUASI-STATIQUE-D%27UNE-CAVITE-A-SYMETRIE-JeanCharlesRogerSalencon/d455eb4c7fa260f8658dfce74198e559776091da (accessed 11.29.20).
Shan, Y., Zhao, H., Zhao, J., Ma, Y., 2018. Numerical simulation of cement interfaces in casing eccentric wells. In: ISRM International Symposium - 10th Asian Rock Mechanics Symposium. International Society for Rock Mechanics and Rock Engineering. Paper Number: ISRM-ARMS10-2018-092.
Therond, E., Bois, A.-P., Whaley, K., Murillo, R., 2017. Large-scale testing and modeling for cement zonal isolation in water-injection wells. SPE Drill. Complet. 32, 290–300. https://doi.org/10.2118/181428-PA.
Thiercelin, M.J., Dargaud, B., Baret, J.F., Rodriquez, W.J., 1998. Cement design based on cement mechanical response. SPE Drill. Complet. 13 (4), 266–273. https://doi.org/10.2118/52890-PA.
Wang, W., Taleghani, A.D., 2014. Three-dimensional analysis of cement sheath integrity around Wellbores. J. Petrol. Sci. Eng. 121, 38–51. https://doi.org/10.1016/j.petrol.2014.05.024.
Xi, Y., Li, J., Liu, G., Tao, Q., Lian, W., 2018. A new numerical investigation of cement sheath integrity during multistage hydraulic fracturing shale gas wells. J. Nat. Gas Sci. Eng. 49, 331–341. https://doi.org/10.1016/j.jngse.2017.11.027.
Yang, Y., 2017. Study on the Fracturing Optimum Design and Effect Evaluation of Deep Shale Gas. Master Thesis. China University of Petroleum (Beijing), Beijing.
Yin, F., Hou, D., Liu, W., Deng, Y., 2019. Novel assessment and countermeasure for micro-annulus initiation of cement sheath during injection/fracturing. Fuel 252, 157–163. https://doi.org/10.1016/j.fuel.2019.04.018.
Zhang, W., Eckert, A., 2020. Micro-annulus generation under downhole conditions: insights from three-dimensional staged finite element analysis of cement hardening and wellbore operations. J. Rock Mech. Geotech. Eng. 12 (6), 1185–1200. https://doi.org/10.1016/j.jrmge.2020.03.003.
Zhang, Z., Wang, H., 2017. Effect of thermal expansion annulus pressure on cement sheath mechanical integrity in HPHT gas wells. Appl. Therm. Eng. 118, 600–611. https://doi.org/10.1016/j.applthermaleng.2017.02.075.